Supporting information for the manuscript

Dilute Gd hydroxycarbonate particles for localized spin qubit integration

Inés Tejedor,[a] Ainhoa Urtizberea,[b] Eva Natividad,[b] Jesús I. Martínez,[a] Ignacio Gascón[a] and Olivier Roubeau[a,*]

a Instituto de Nanociencia y Materiales de Aragón (INMA), CSIC – Universidad de Zaragoza, Plaza San Francisco s/n, 50009, Zaragoza, Spain. E-mail: roubeau@unizar.es

b Instituto de Nanociencia y Materiales de Aragón (INMA), CSIC – Universidad de Zaragoza, Campus Río Ebro, María de Luna 3, 50018 Zaragoza, Spain.

Table of contents

Synthetic details

$YCl_3 \cdot 6H_2O$, $GdCl_3 \cdot 6H_2O$ and Reagent/HPCL grade solvents were purchased from Aldrich and used without further purification. Pure urea was purchased from Panreac.

Synthesis was carried out adapting the conditions previously reported for the pure Ln hydroxycarbonate particles.[1] Specifically, $YCl_3 \cdot 6H_2O$, $GdCl_3 \cdot 6H_2O$ and urea, in varying amounts depending on the targeted composition and size (see Table S1), were added to 10 mL milliQ water in 30 mL thick borosilicate tubes with hermetic caps. After the dispersions were homogenized through bath ultrasonication, the tubes were closed, heated to 100ºC in an oven, and kept at this temperature for 90 min. After cooling, the white solids were recovered by centrifugation, washed 5 times with milliQ water, and dried in ambient air. Yields were in the range 51-72%. The Gd and Y contents of the doped samples were determined by ICP-AES on the larger particles giving the Gd/Y ratios given in Table S1. All samples gave C, H analysis in good agreement with the $Gd_xY_{1-x}OHCO_3 \cdot yH_2O$ formula, with y in the range 0.3-0.8.

Dispersions in MeOH were obtained using ultrasonication with a probe-type device Hielscher UP400S (Power output 400 W) equipped with an H3 type tip (3 mm diameter). The optimal conditions were 30 min ultrasonication at 50% amplitude. $MeOH:CHCl_3$ suspensions were then prepared from the MeOH suspensions, but no further tip ultrasonication. Dispersions in DMF were made by bath ultrasonication for 30 min.

Table S1. Reagents amounts, yields and Gd/Y ratio derived from ICP-AES for the synthesis of $Gd_xY_{1-x}OHCO_3$ small and large particles. The Gd/Y ratios derived indirectly from scaling of *M vs. H* data (see Fig. S7) are also given.

aimed composition aimed diameter	$Gd_{0.1}Y_{0.9}$ 100 nm	$Gd_{0.01}Y_{0.99}$ 100 nm	$Gd_{0.001}Y_{0.999}$ 100 nm	$Gd_{0.1}Y_{0.9}$ 300 nm	$Gd_{0.01}Y_{0.99}$ 300 nm	$Gd_{0.001}Y_{0.999}$ 300 nm
$YCl_3 \cdot 6H_2O$ (mg)	40.22	40.14	40.06	38.65	39.86	39.61
$GdCl_3 \cdot 6H_2O$ (mg)	4.88	0.51	0.08	4.72	0.49	0.06
urea (mg)	594.14	590.94	594.96	289.03	285.79	297.48
used Gd/Y ratio	0.10	0.010	0.0016	0.10	0.010	0.0012
yield (mg)	15.94	16.46	7.95	12.38	11.23	12.15
found Gd/Y ratio (ICP)	-	-	-	0.099	0.007	0.003
Gd/Y ratio (*M vs. H*)	0.0917	0.0099	0.0021	0.0937	0.0065	0.0026

---

[1] E. Matijevic and W. P. Hsu, *J. Coll. Interf. Sci.*, **1987**, 118, 506-523

Langmuir and Langmuir−Blodgett film fabrication

Surface pressure−area (π−A) isotherms were obtained using a Teflon Langmuir trough NIMA model 702 (dimensions 720 mm x 100 mm).

Brewster Angle Microscopy (BAM) images were acquired using a KSV NIMA Micro BAM equipped with a red laser (659 nm, 50 mW) as the light source. The incidence angle was fixed at 53.1°, and a black quartz plate was placed inside the trough as a light trap. The optics of the system provided a spatial resolution of 6 μm per pixel in the water surface plane and a field of view of 3600x4000 μm^2.

Langmuir-Blodgett films were made with a KSV-NIMA trough model KN 2003, with dimensions of 580 mm × 145 mm.

In all cases, compression was performed by a symmetric double-barrier system at constant speed of 8 cm^2·min^{-1}. Surface pressure was continuously monitored during the experiments by means of a Wilhelmy balance using a filter paper plate. The troughs are housed in a clean room inside closed cabinets and the room temperature is maintained at 293 K (±1 K). Ultra-pure Milli-Q water (ρ = 18.2 MΩ·cm) was employed as subphase. In all experiments, the trough was carefully cleaned with acetone and chloroform, filled and emptied twice with Milli-Q water and ultimately filled with Milli-Q water. The subphase was then carefully cleaned by closing the barriers down to 40 mm distance and mild surface-touch vacuuming intra-barriers area. After opening the barriers to the maximum area, the system was let to equilibrium for 5 minutes. The Gd$_x$Y$_{1-x}$OHCO$_3$ dispersion was carefully spread drop-by-drop onto the subphase using a Hamilton microsyringe held very close to the subphase surface, and left to evaporate for 20 minutes before starting the compression. Substrates (Si wafer) were cleaned by ultrasonication, successively in chloroform, acetone and ethanol. Transfers were carried out by vertical-dipping at various surface pressures, the substrate, initially immersed in the subphase, being raised at 1 mm·min^{-1}.

Localized particle deposition

Nanoparticles direct writing onto specific locations of a surface can be conducted by Nanolithography. However, most materials deposited by using scanning-probe lithography techniques are molecules, thanks to their ability to diffuse. Liquid inks of e.g. polymers are also disposed by using these techniques, the transfer resulting from a growth of an ink droplet that gets snapped off upon tip retraction. Reports of nanoparticles deposition by nanolithography are relatively scarce, and limited to nanoparticle sizes up to 10 nm. To the best of our knowledge, deposition of particles with diameters in the range of 300 nm into specific locations using dip-pen nanolithography has not been reported.

Here, deposition experiments conducted using dip-pen nanolithography showed that the size of the Gd$_x$Y$_{1-x}$OHCO$_3$ particles does not allow their transport to be controlled by diffusion. Instead, transference was achieved as a liquid ink composed of particles suspended in a carrier liquid, and evaporation of the ink solvent. Deposition is therefore conducted by meeting the cantilever to the substrate. Two techniques have been employed.

Dip-Pen Nanolithography (DPN)

Experiments were performed on a DPN 5000 system (NanoInk, USA) with ORC8 Si3N4 Bruker probes, using the D cantilever with spring constant k = 0.05 N/m. Tips were coated by loading 0.7 μL droplet ink (0.5 mg mL^{-1} in DMF) onto a silicon substrate and subsequent drying for about 10 min. After this time the droplet looked nearly, but not completely, dried. Then, tips were dipped into the remaining droplet, by approaching the

cantilever until it gleamed. After shedding excess ink on a sacrificial area writing some arbitrary patterns, the tip array was moved into position and lines were written using a speed of 0.2 mm s^{-1} at a humidity of 37 % R. H.

Atomic Force Microscope (AFM)

Experiments were performed on an Ntegra Aura NT-MDT microscope in contact mode with the same cantilever and ink as for DPN. Tips were now coated by drop-casting 40 μL ink and drying in air for 24 h to allow high tip loading. Before proceeding with the deposition, and additional 40 μL of ink was drop-casted and let for about 5-10 min to grant the ink fluidity. After shedding excess ink on a sacrificial area, the cantilever was approached in contact mode until the deflection signal showed contact of the tip. Subsequent approach of the tip was conducted slowly until a slight gleaming of the cantilever was visible. The cantilever was then lifted off the substrate rapidly. Experiments were conducted under a humidity of 40 % R. H.

Physical characterization

C, H analyses were performed by using a Perkin-Elmer EA-2400 Series II analyser at the Elemental Analysis service of CEQMA. *Metal analyses* were performed through Inductively Coupled Plasma – Atomic Emission Spectrosocpy (ICP-AES) at the Mikroanalytisches Labor Pascher Laboratory, Germany.

Powder X-ray diffraction data were obtained at ambient temperature using a Rigaku D-Max diffractometer equipped with a rotating anode and a graphite monochromator to select the Cu-Kα wavelength, through the Servicio General de Apoyo a la Investigación-SAI, Universidad de Zaragoza.

Infra-red spectra were acquired on neat samples using a Perkin Elmer Spectrum 100 apparatus equipped with an ATR device.

Scanning Electron Microscopy observations were made through the Laboratorio de Microscopías Avanzadas (LMA) with an FEI INSPECT-F50 microscope working at 10 kV. Samples were coated with conductive layer of Pt.

Magnetic measurements were performed with a commercial magnetometer equipped with a SQUID sensor hosted by the Physical Measurements Unit of the Servicio General de Apoyo a la Investigación-SAI, Universidad de Zaragoza. The diamagnetic contributions to the susceptibility were corrected using Pascal's constant tables. Direct current (dc) data were collected between 2 and 300 K with an applied field of 100 Oe and at low temperature up to 5 T.

Electron Paramagnetic Resonance (EPR) experiments, both continuous wave (cw) and pulsed time domain (TD), were performed with a Bruker Biospin ELEXSYS E-580 spectrometer operating in the X-band, using a gas-flow Helium cryostat for low-temperature experiments. cw and echo-detected field-swept (EDFS) EPR spectra were recorded respectively at room temperature and 6 K. 2p Hahn-echo and Inversion Recovery ESE-detected experiments were performed at various temperatures from 6 to 20 K and fields from 1000 to 5000 G. In these experiments the length of the π/2 pulse was, typically, 16 ns whereas the length of the π pulse was 32 ns. The simulated cw-EPR spectrum was obtained with the EasySpin program[2].

Dynamic Light Scattering (DLS) experiments were conducted using a Malvern Zetasizer Nano ZS ZEN3600 equipped with a 633 nm laser and configured in a back-scattering arrangement at 173º. Measurements were done at 25ºC.

X-ray Photoelectron Spectroscopy (XPS) analyses were performed through the Laboratorio de Microscopias Avanzadas (LMA) with a Kratos AXIS ultra DLD spectrometer with a monochromatic Al Kα X-ray source (1486.6 eV) using a pass energy of 20 eV. The photoelectron take-off angle was 90° with respect to the sample plane. The data treatment was done using CasaXPS software. Shirley or Offset-Shirley backgrounds were used. The binding energy (BE) scales are internally referenced to the C 1s adventitious carbon peak at 284.8 eV.

---

[2] Stefan Stoll and Arthur Schweiger. *J. Magn. Reson.*, 2006, **178**, 42-55
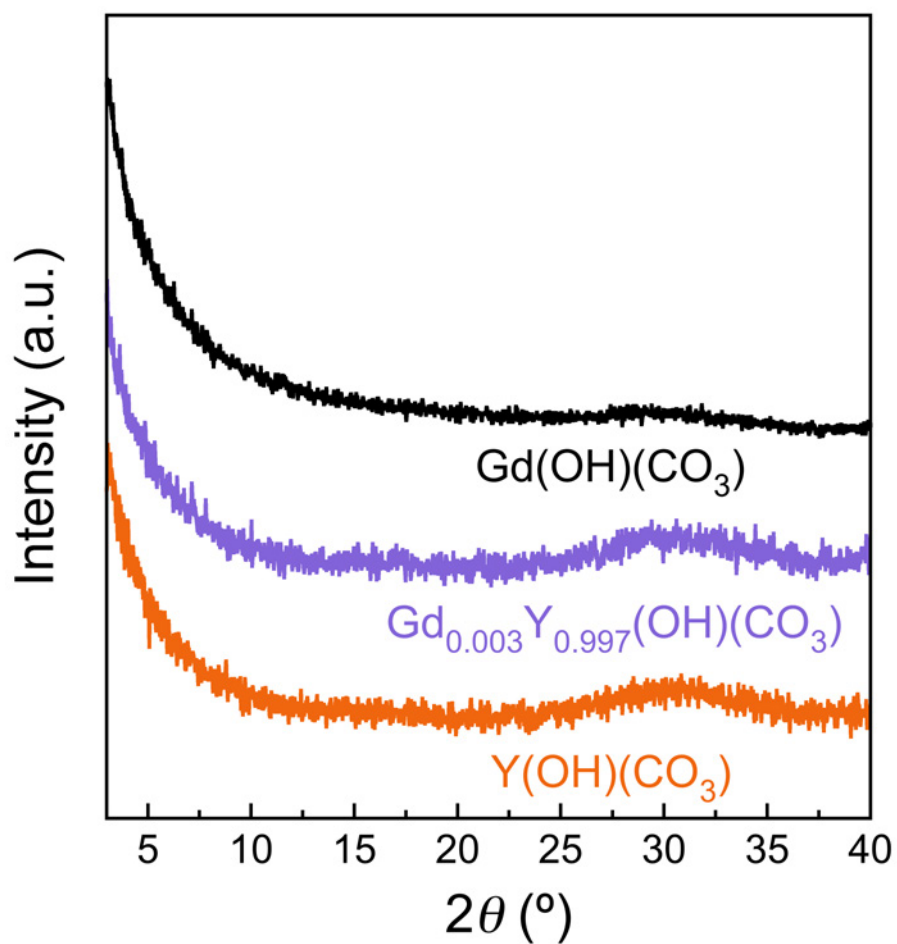
Figure S1. Powder X-Ray diffraction patterns for the $Gd_{0.003}Y_{0.997}OHCO_3$ particles, compared with those of the pure Y and Gd materials, as indicated.
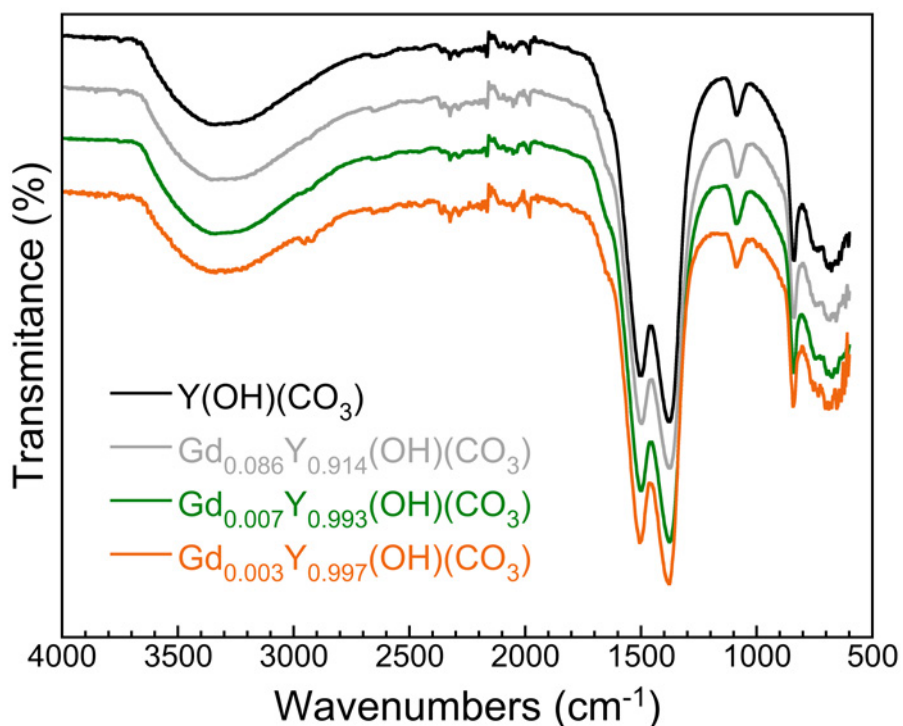
Figure S2. FT-IR spectra of the obtained $Gd_xY_{1-x}OHCO_3$ particles, showing the characteristic carbonate C–O bands: ν_3 at 1502 and 1377 cm^{-1}, ν_1 at 1088 cm^{-1} and ν_2 at 839 cm^{-1}. The shoulder at *ca.* 1645 cm^{-1} likely corresponds to the deformation band of hydration water, while O–H stretchings vibrations of both water and hydroxyl groups appear in the form of a broad band covering the 3000-3500 cm^{-1} range. Y–O and Gd–O bands are not visible in our experimental window.
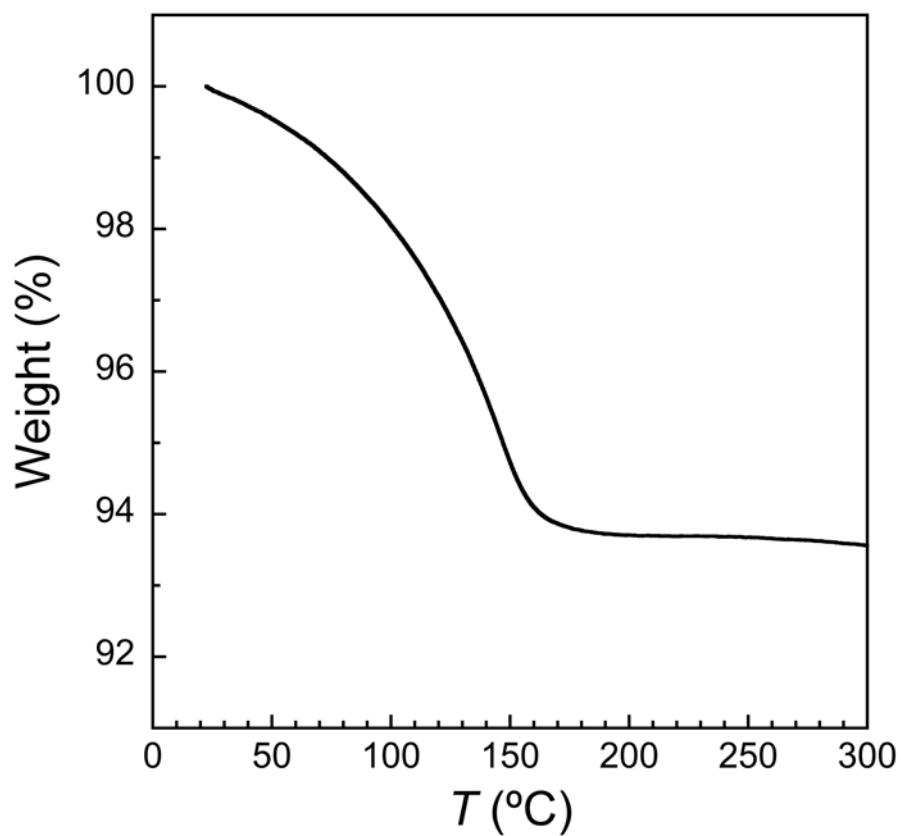
Figure S3. Typical thermogravimetric data for the obtained $Gd_xY_{1-x}OHCO_3$ particles. The data shown corresponds to x = 0. The weight loss of *ca.* 6.3 % at 200ºC agrees well with *ca.* 0.8 molecules of water per formula unit.
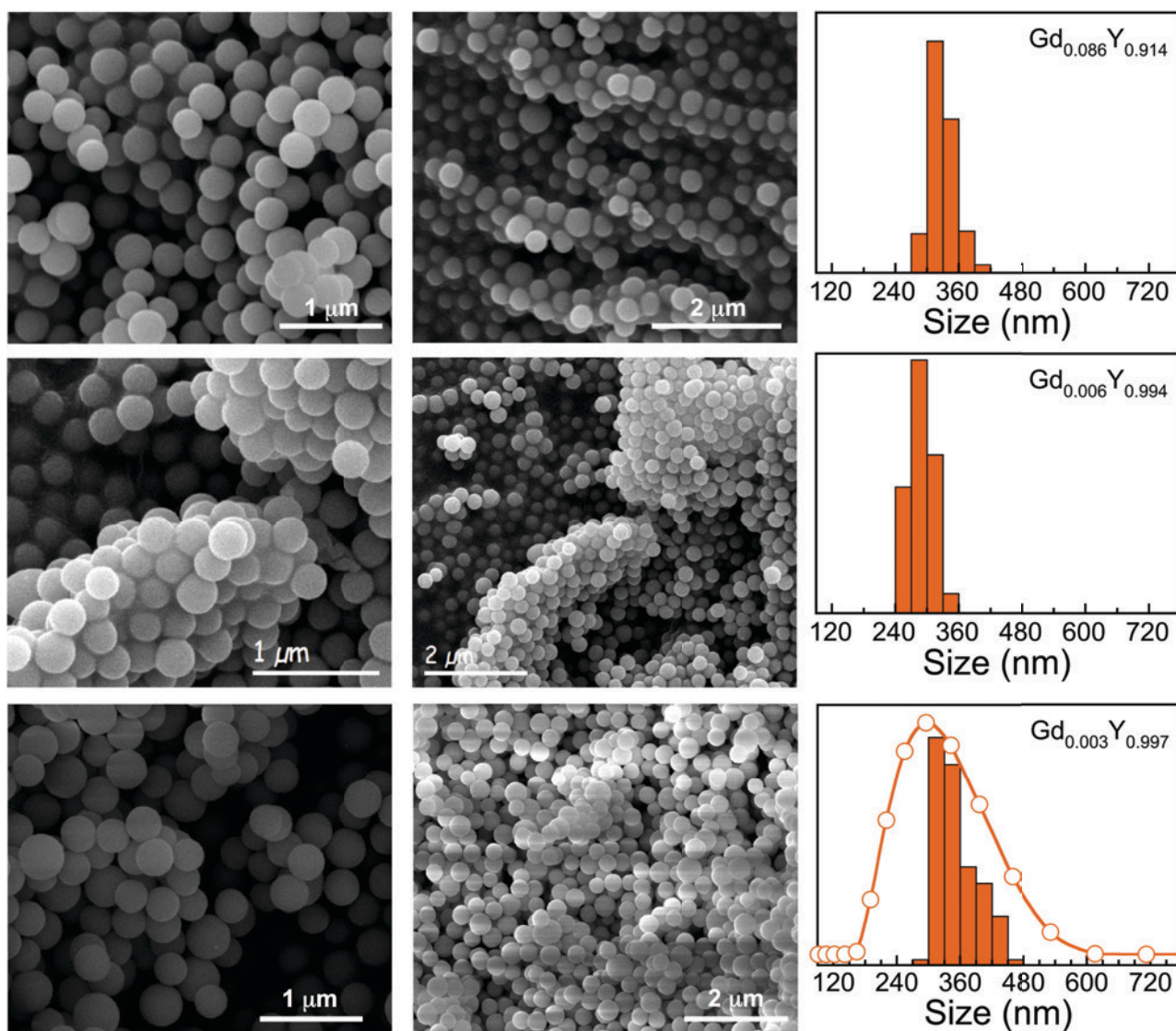
Figure S4. SEM images at two magnifications (left and middle) and corresponding size distribution histograms (right, bars) together with DLS hydrodynamic size distribution (empty circles with line) of large $Gd_xY_{1-x}OHCO_3$ particles, as indicated (x as determined by ICP). DLS measurements were made on a MeOH 1.5 mg/mL dispersion.
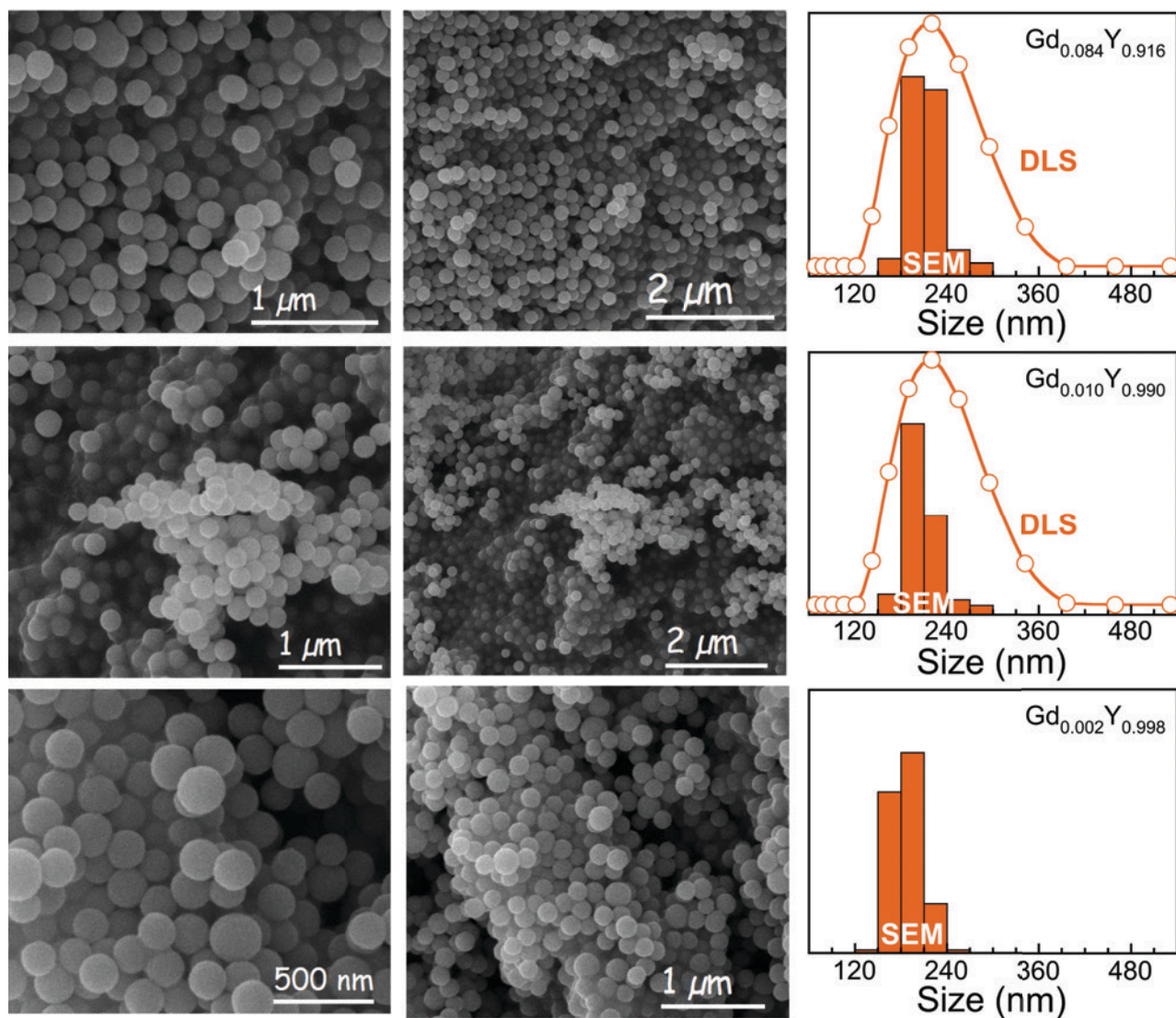
Figure S5. SEM images at two magnifications (left and middle) and corresponding size distribution histograms (right, bars) together with DLS hydrodynamic size distributions (empty circles with line) of small $Gd_xY_{1-x}OHCO_3$ particles, as indicated (x determined from scaling of *M vs. H* data). DLS measurements were made on MeOH 1.5 mg/mL dispersions.
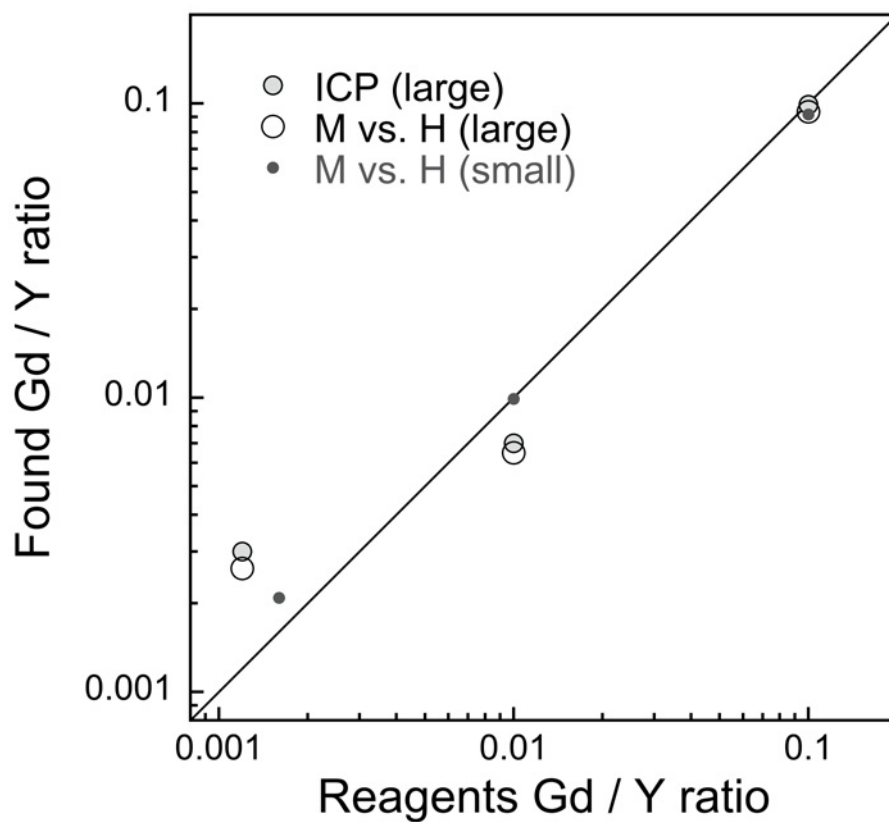
Figure S6. Gd/Y ratio derived from ICP-AES (large grey circles) and scaling of *M vs. H* data (large empty circles for the larger particles and small grey circles for the smaller particles) as a function of Gd/Y ratio of the used reagents.
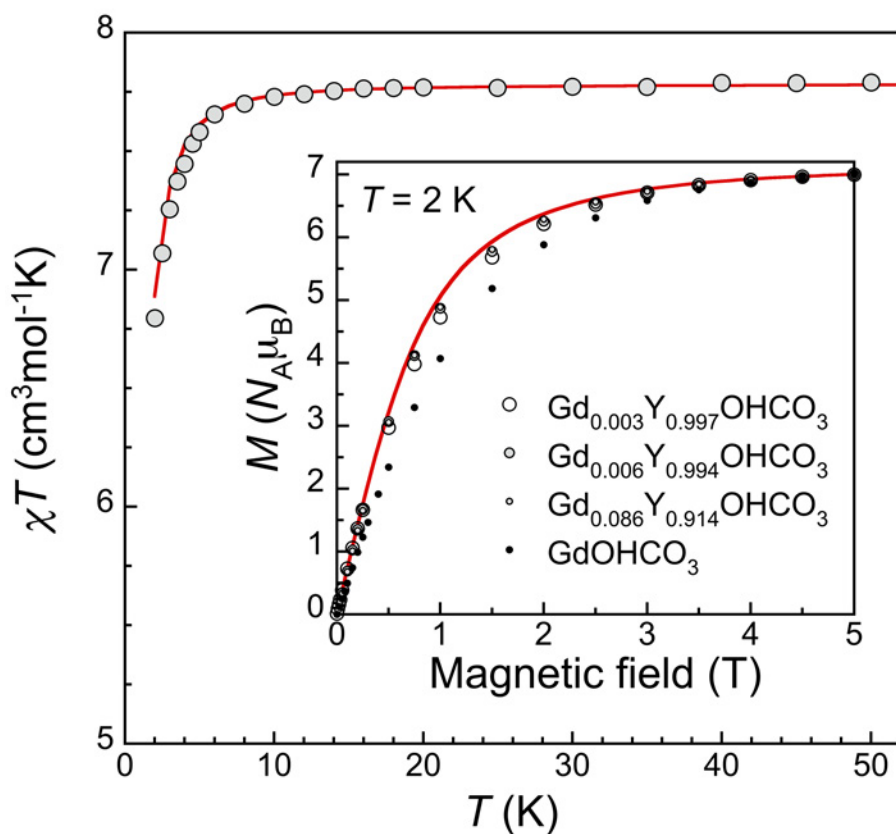
Figure S7. Temperature dependence of the product χT for the $Gd_{0.007}Y_{0.993}OHCO_3$ large particles as derived from dc measurements at 0.5 T and scaled to pure $GdOHCO_3$. The solid red line corresponds to the curve calculated with the *curry* function of Easyspin[2] with the same parameters as those used to simulate the cw-EPR spectrum (see text). Inset: Magnetization isotherms at 2 K for $Gd_xY_{1-x}OHCO_3$ large particles as indicated. The red line is the Brillouin function for $S = 7/2$ and g = 2.02. The data are scaled to pure $GdOHCO_3$, whose data are also shown for comparison.
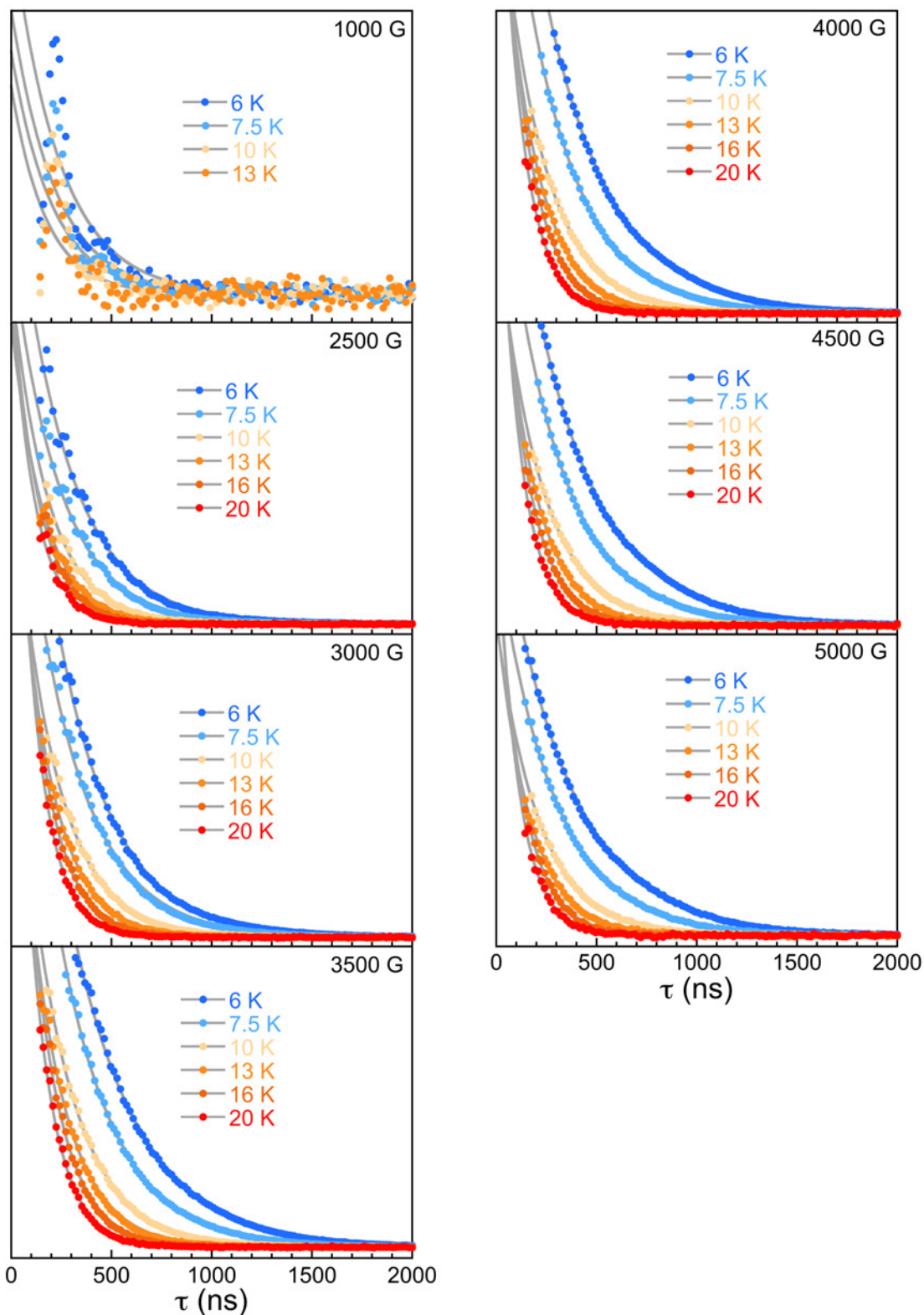
Figure S8. 2p ESE intensity as a function of inter-pulse interval, τ, for $Gd_{0.003}Y_{0.997}(OH)(CO_3)$ 330 nm particles at the indicated applied magnetic fields and increasing temperatures (circles). Grey lines correspond to the evolution predicted with an exponential decay expressed as:

$$y(\tau) = y_0 + A_{2p}e^{-2\tau/T_M}$$

with the values of the parameters that give the best fit gathered in Table S2.
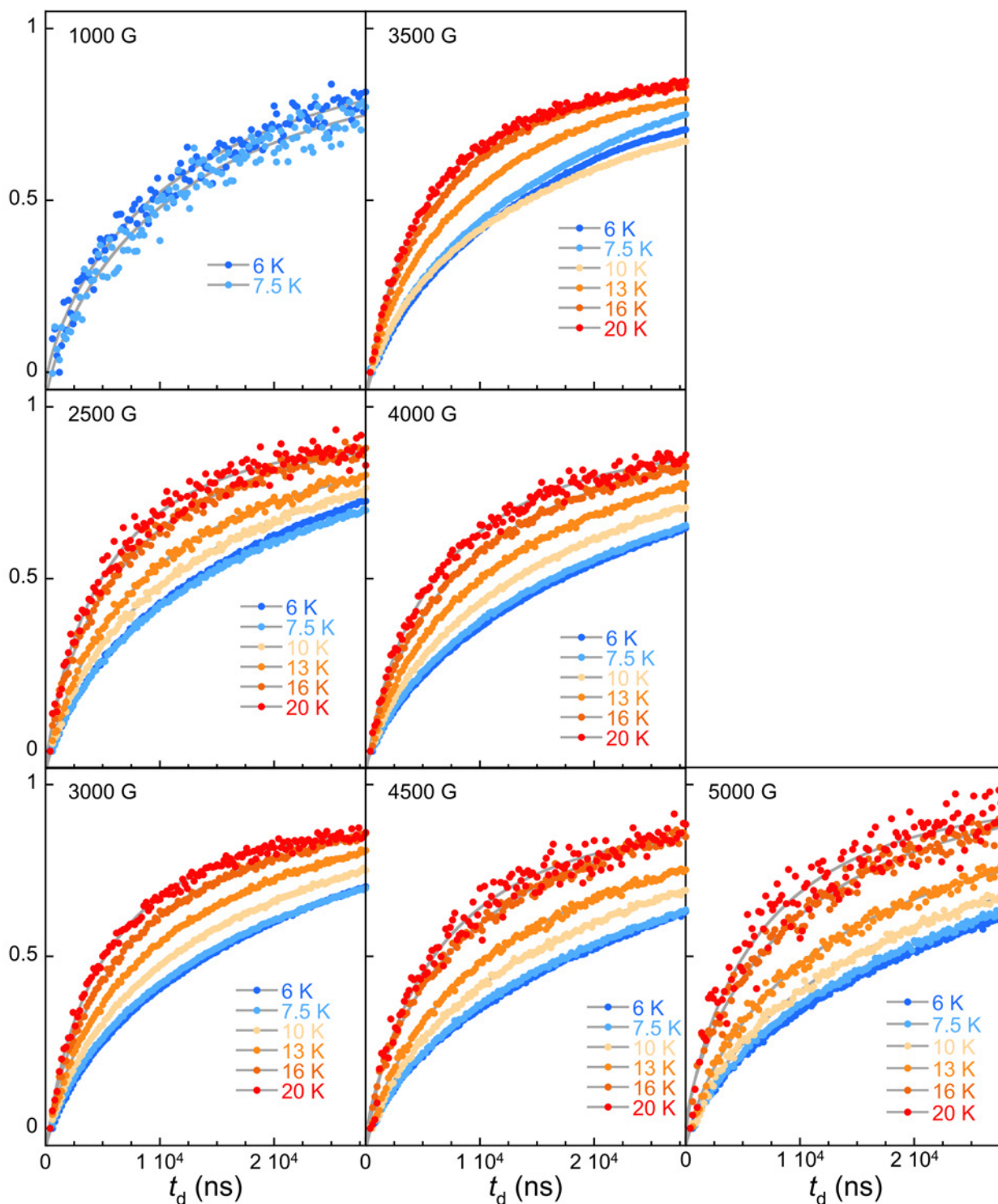
Figure S9. Normalized ESE detected Inversion Recovery as a function of delay time, t_d, for $Gd_{0.003}Y_{0.997}(OH)(CO_3)$ 330 nm particles at the indicated applied magnetic fields and increasing temperatures (circles). Grey lines correspond to a stretched exponential t_d dependence modeled by:

$$y(t_d) = y_\infty - y_0 e^{-\left(t_d/\beta T_1'\right)^\beta}$$

that best fit to the data. The stretched exponent β was first let free, and then fixed to avoid over-parametrization. The values of the relevant best-fit parameters are gathered in Table S2.
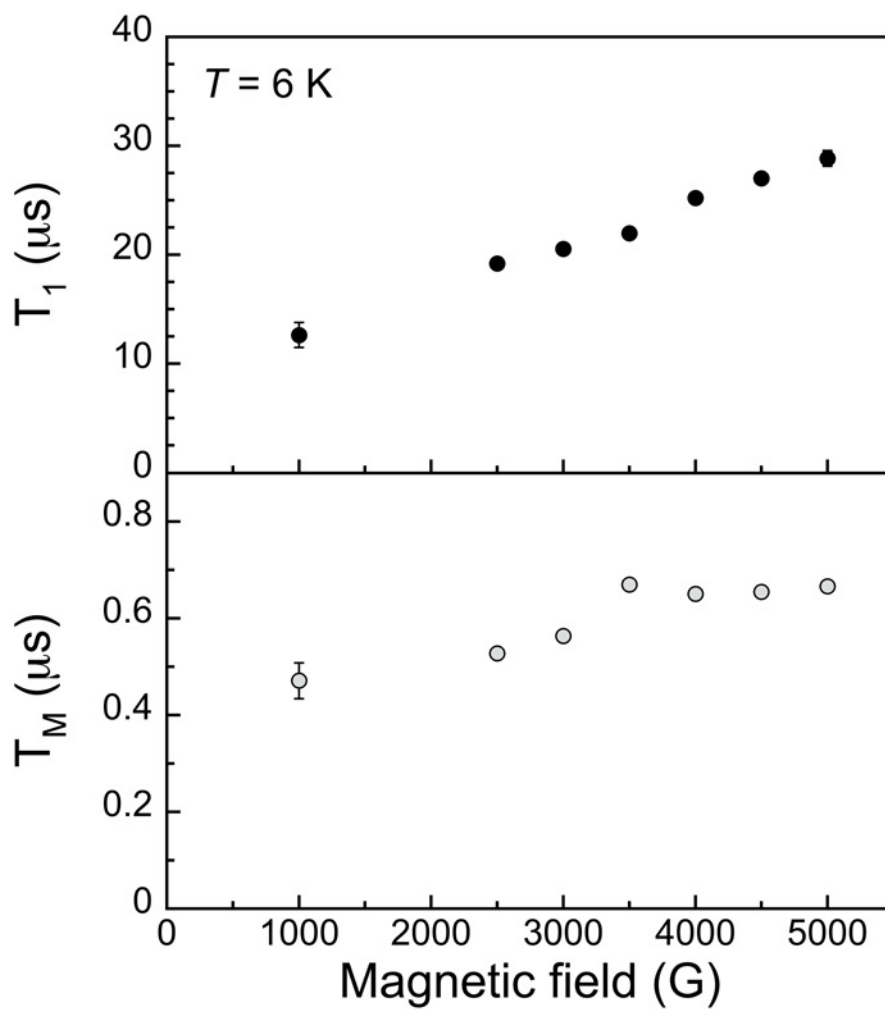
Figure S10. Mean longitudinal relaxation time T_1 and phase memory time T_M for $Gd_{0.003}Y_{0.997}(OH)(CO_3)$ 330 nm particles at 6 K.

Table S2. Parameters that provide the best fits to ESE detected Inversion Recovery signals and the 2p-ESE decay for $Gd_{0.003}Y_{0.997}(OH)(CO_3)$ 330 nm particles.

T (K)	H (G)	T_M (µs)	T_1' (µs)	β
6	1000	0.47(4)	16.8(15)	0.75
	2500	0.528(9)	25.6(3)	0.75
	3000	0.564(3)	27.4(3)	0.75
	3500	0.670(5)	31.4(5)	0.70
	4000	0.650(2)	33.6(3)	0.75
	4500	0.655(2)	36.0(7)	0.75
	5000	0.666(2)	38.5(10)	0.75
7.5	1000	0.44(4)	16.7(17)	0.75
	2500	0.477(7)	22.6(3)	0.75
	3000	0.511(3)	23.7(2)	0.75
	3500	0.557(2)	31.4(2)	0.70
	4000	0.541(1)	28.3(3)	0.75
	4500	0.553(1)	30.8(5)	0.75
	5000	0.559(1)	31.2(9)	0.75
10	1000	0.38(3)	12.9(21)	0.75
	2500	0.397(6)	17.9(3)	0.75
	3000	0.415(2)	18.9(2)	0.75
	3500	0.473(4)	24.4(2)	0.70
	4000	0.430(1)	22.5(3)	0.75
	4500	0.432(1)	23.8(5)	0.75
	5000	0.423(1)	25.5(9)	0.75
13	1000	0.30(1)	-	-
	2500	0.324(5)	13.7(3)	0.75
	3000	0.338(2)	14.4(2)	0.75
	3500	0.370(3)	14.0(1)	0.75
	4000	0.343(2)	16.8(2)	0.75
	4500	0.330(1)	17.6(4)	0.75
	5000	0.334(2)	18.5(7)	0.75
16	2500	0.272(5)	10.4(3)	0.75
	3000	0.280(2)	10.6(2)	0.75
	3500	0.306(2)	9.63(7)	0.75
	4000	0.279(1)	12.4(2)	0.75
	4500	0.272(2)	13.5(4)	0.75
	5000	0.261(2)	14.2(8)	0.75
20	2500	0.233(4)	7.8(3)	0.75
	3000	0.226(2)	7.6(2)	0.75
	3500	0.232(2)	7.4(1)	0.75
	4000	0.230(2)	9.2(3)	0.75
	4500	0.218(1)	9.0(5)	0.75
	5000	0.213(3)	9.6(9)	0.75
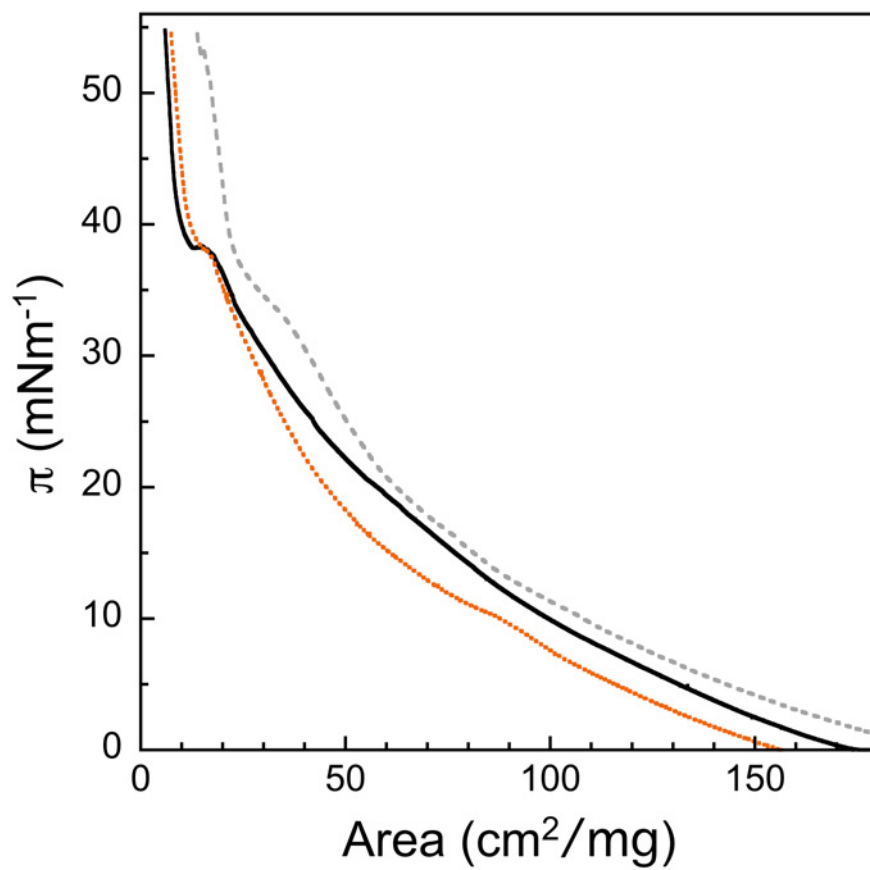
Figure S11. Surface pressure−area (π−A) isotherms obtained for three batches of $Gd_xY_{1-x}OHCO_3$ particles with different sizes and/or composition.

HV	spot	mag	det	mode	WD	HFW	tilt	⸺ 10 µm ⸺
10.00 kV	3.0	5 000 x	ETD	SE	11.5 mm	59.7 µm	0 °	LMA
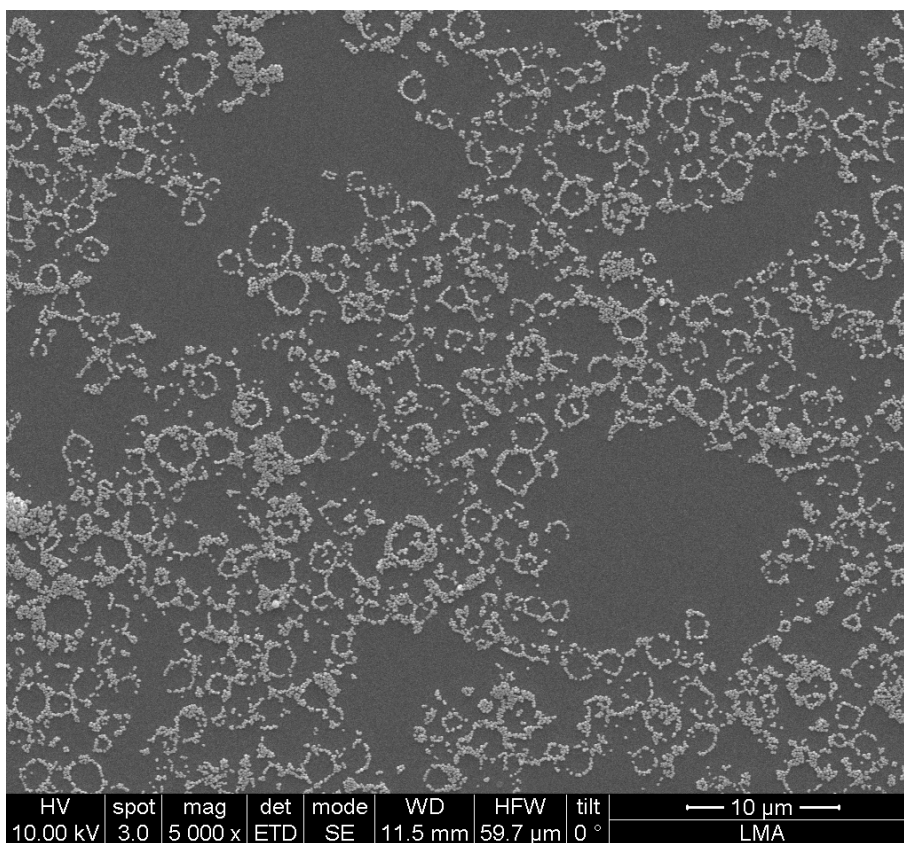
Figure S12. SEM image of a LB film obtained upon vertical transfer of large particles onto a Si wafer at 10 mN/m.

HV	spot	mag	det	mode	WD	HFW	tilt	50 μm
10.00 kV	3.0	1 500 x	ETD	SE	9.8 mm	199 μm	0 °	LMA
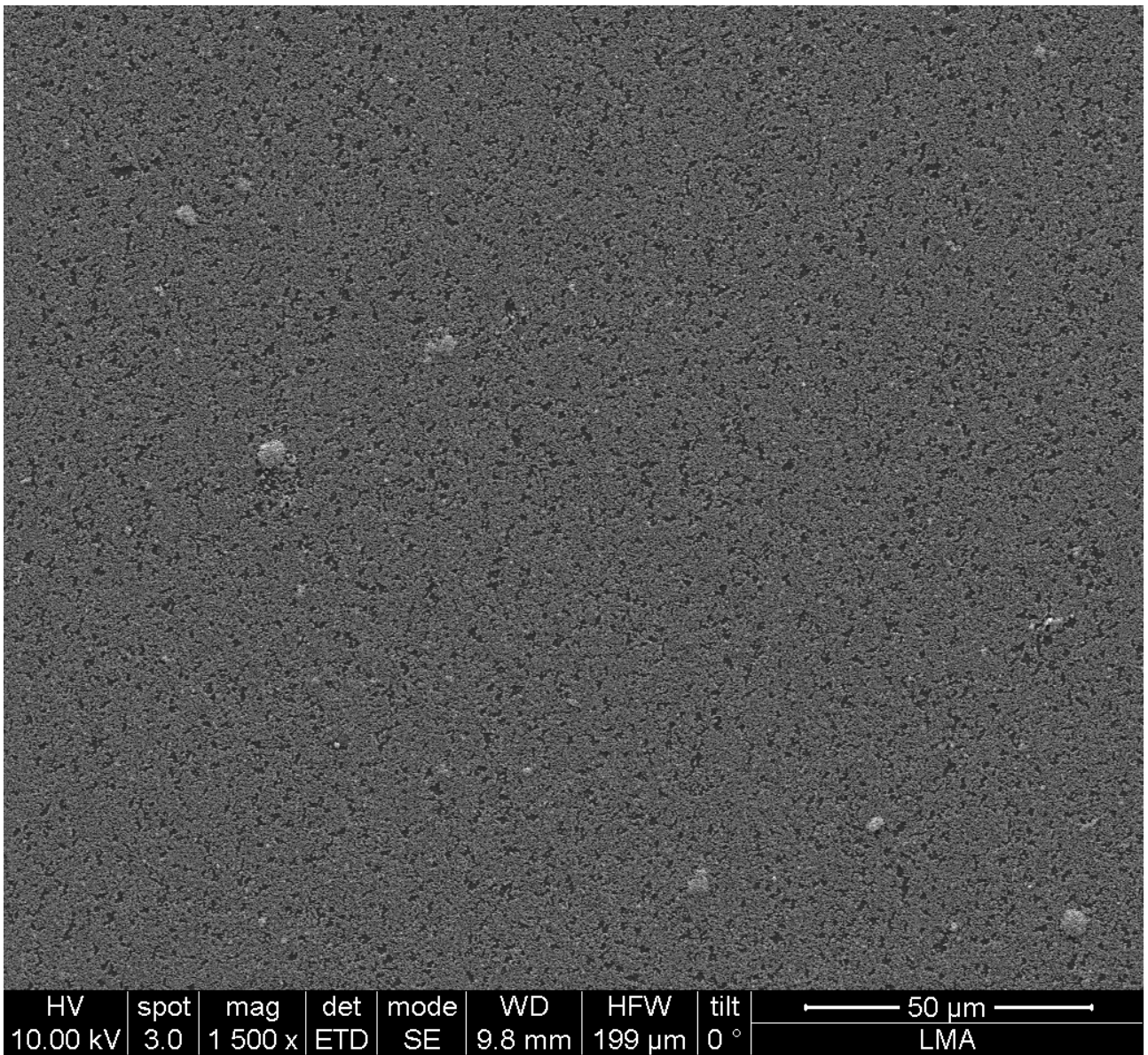
Figure S13. Large area SEM observation of a LB film obtained upon vertical transfer of large particles onto a Si wafer at 55 mN/m.
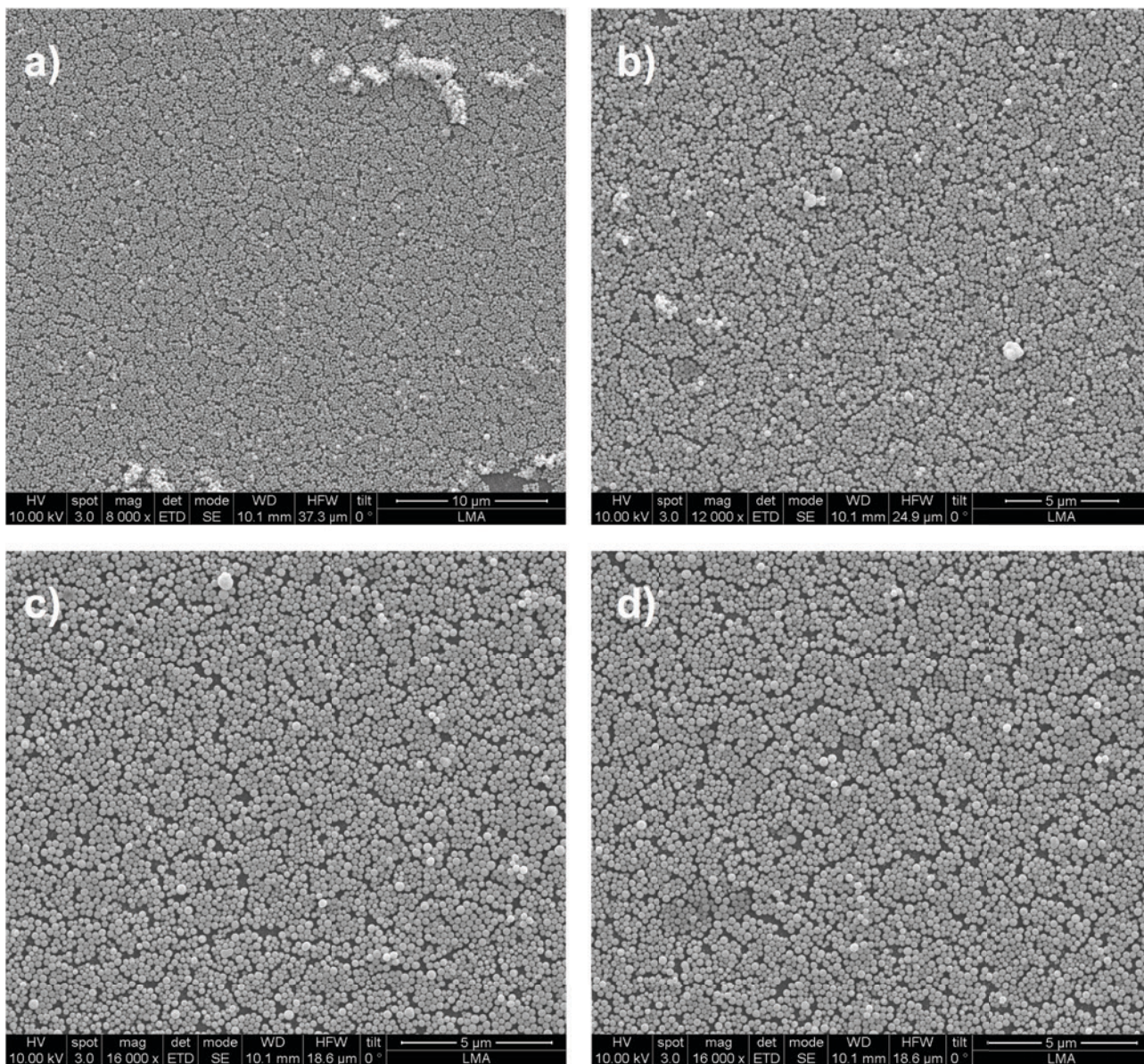
Figure S14. SEM images of various areas of the LB film obtained upon vertical transfer of 222(31) nm particles onto Si wafer at 55 mN/m, at various magnifications.
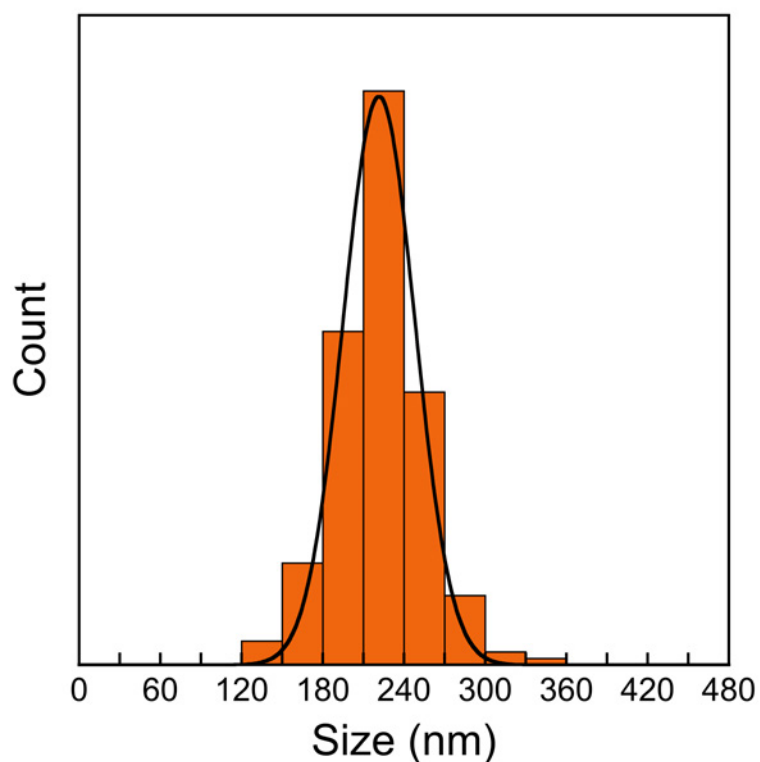
Figure S15. Size distribution histograms of the particles in optimized LB deposits on Si (Fig. S14). Total number of particles measured is 643. The full line is a fit to a Gaussian distribution yielding 222(37) nm in good agreement with the numerical median(sd) of 221(31) nm.
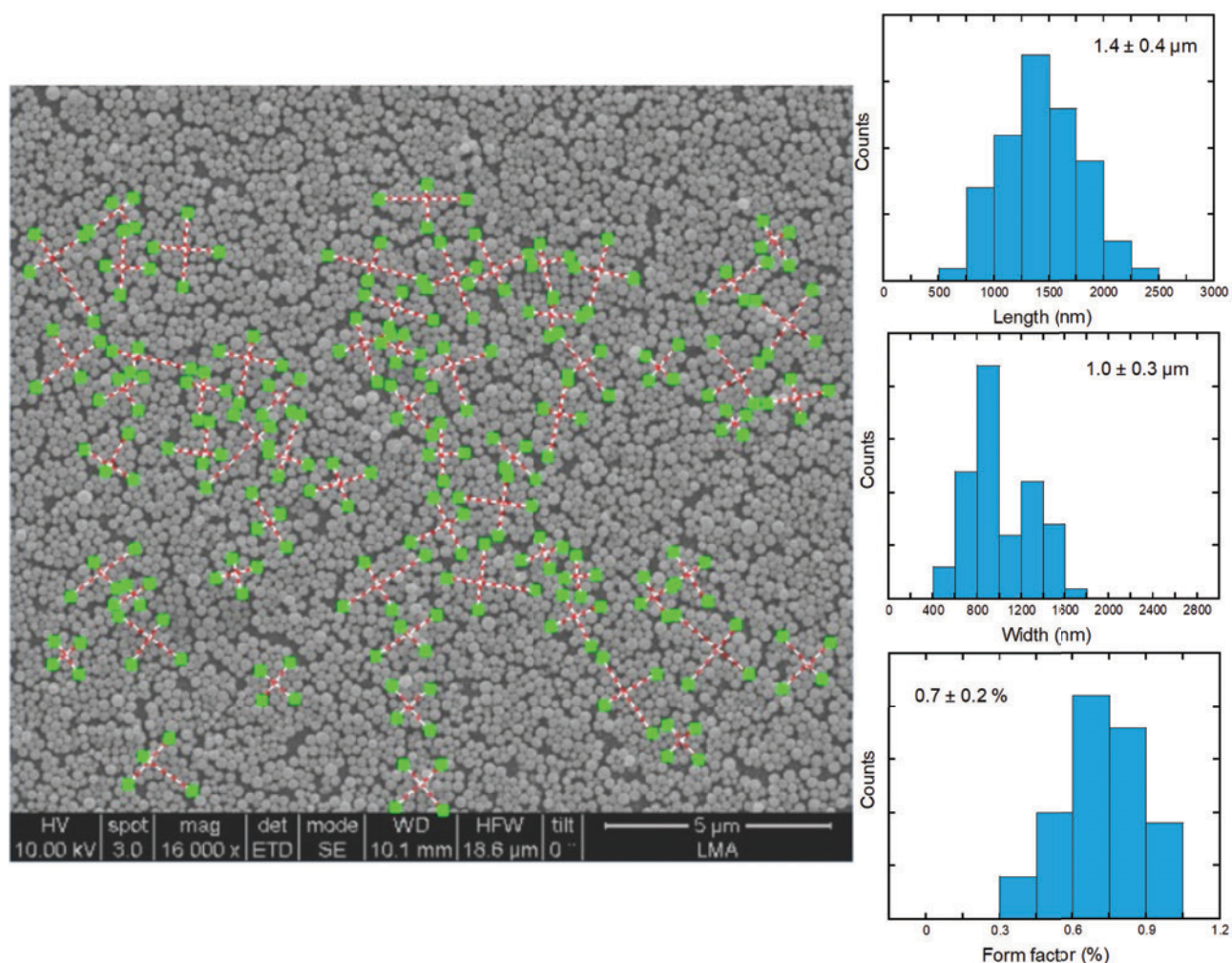
Figure S16. Analysis of SEM images of LB deposits on Si: packed particles domains. To estimate an average domain size, the length and width of 62 of the observed domains were measured (left). Histograms of length, width and form factor are shown on the right, together with mean values and standard deviations. From these results, an average number of particles per domain can be estimated. Assuming identical and spherical particles, the planar particle density for perfect hexagonal arrangements is 90.7%. Considering the mean diameter of 222 nm determined in Fig. S15, the nº of particles of an average rectangular domain of 1.4 x 1.0 μm^2 can be calculated as the domain area multiplied by the planar density and divided by the particle biggest section (circle), giving a mean value of 33 particles per domain. Given that domains are not strictly rectangular, this number is an average upper limit. For perfect square arrangements, the planar particle density is 78.5%. Calculating as previously, a mean value of 28 particles per domain is obtained, again as average upper limit for this kind of arrangement.
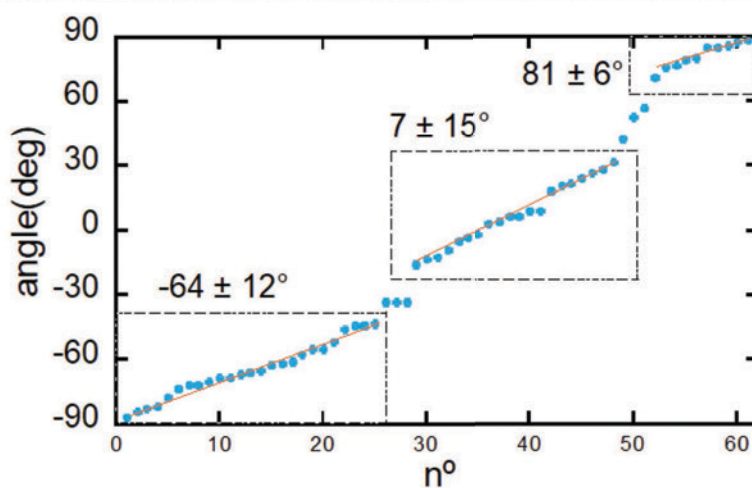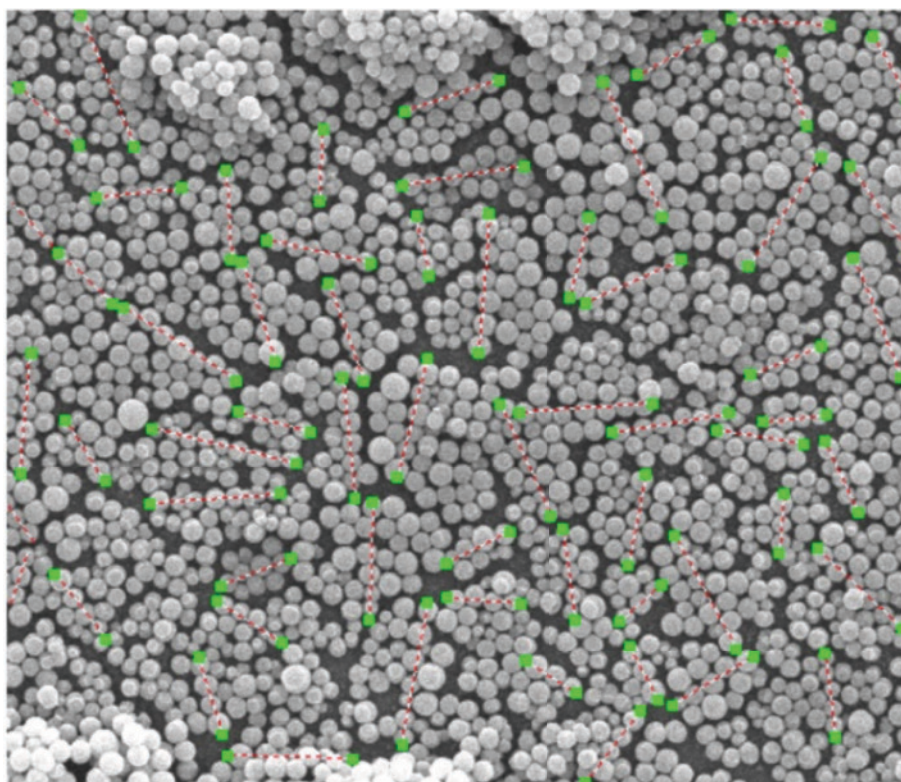
Figure S17. Analysis of SEM images of LB deposits on Si: possible long-range order among domains. The domain orientations were evaluated by measuring the angle of one characteristic particle row per domain (top), and plotting the obtained angles in ascending order (bottom). If a perfect hexagonal arrangement is present, three characteristic angles should be found, tilted 60°. In the plot, three different regions can be observed, but angle dispersion is high, some lower in the 81° orientation, and differences between average values are not strictly 60°. Accordingly, long order may be discarded, although results may be indicative of local imperfect hexagonal order.
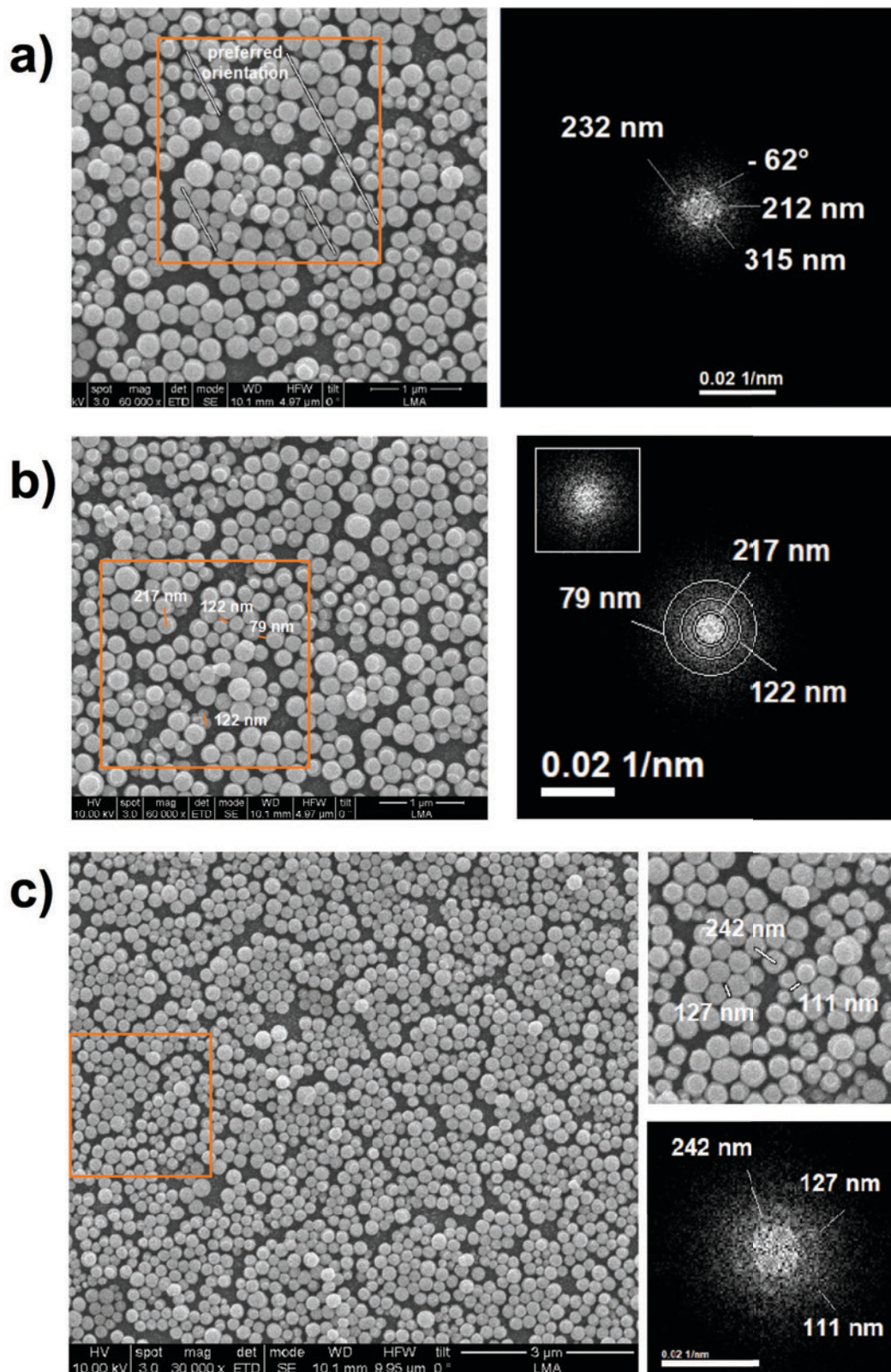
Figure S18. Analysis of SEM images of LB deposits on Si: local order in small areas. The absence of long-range order is reflected in the lack of intense reciprocal lattice points in the FFT analysis of SEM images. In example (a), the FFT detects one preferred orientation (-62°) at the intersection of three domains, with inter-particle distances of 212, 232 and 315 nm. In example (b), however, no preferred orientation is highlighted by the FFT. Instead, weak reciprocal points appear along three rings, with distances corresponding to the spaces between particles (79 nm), to a characteristic inter-particle space of the hexagonal lattice (122 nm, theoretically 73% of particle size) and/or the inter-

particle distances between small (122 nm) and large (217 nm) particles. In example (c), also shown in Figure 3 of the main manuscript, the more similar particle size of the arrangement allows obtaining reciprocal points in quasi-hexagonal arrangement, with distances corresponding to the same characteristic inter-particle space of the hexagonal arrangement (111 and 127 nm) and the inter-particle distances between large (242 nm) particles.
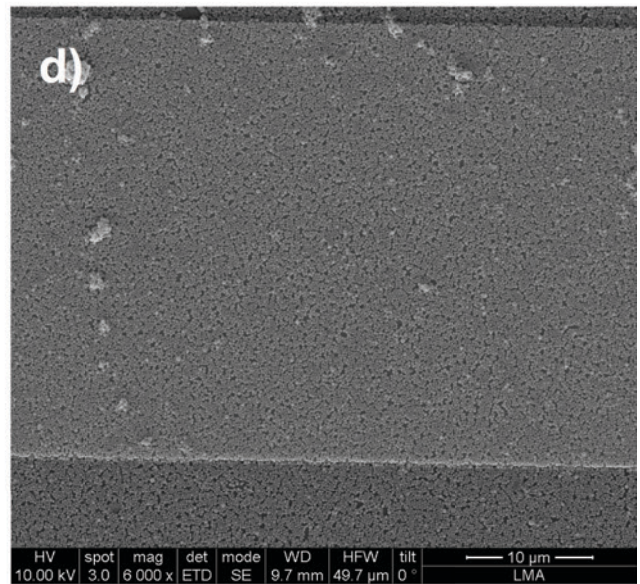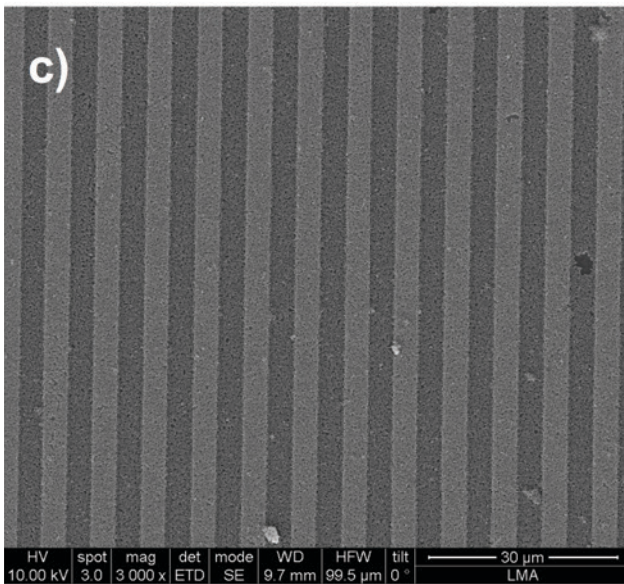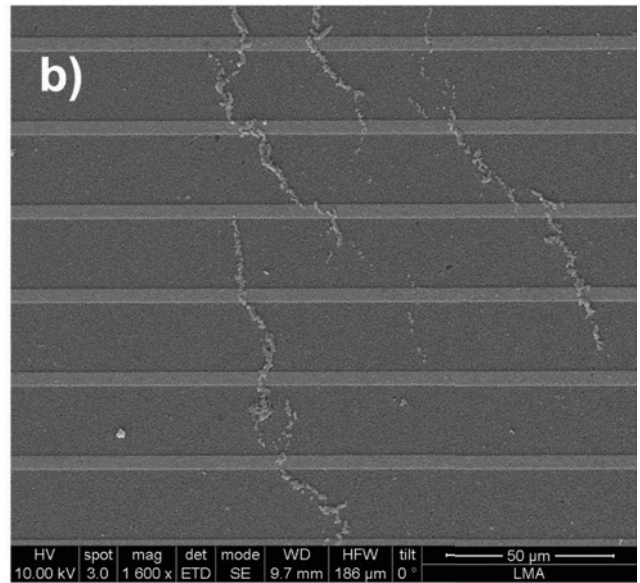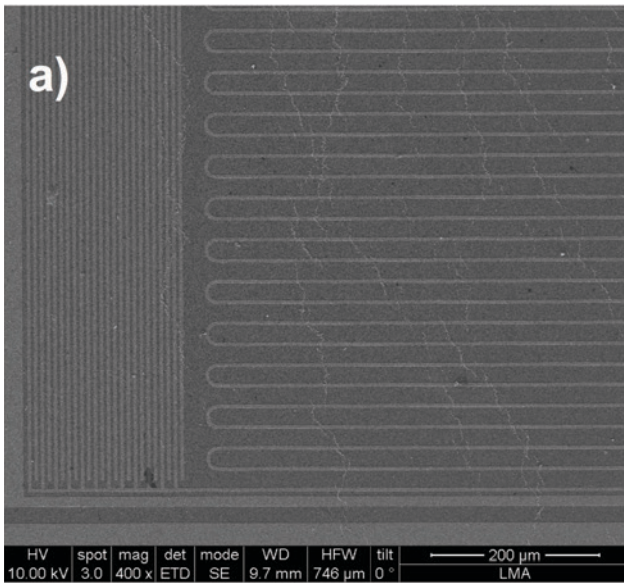
Figure S19. SEM images of various areas of the LB film obtained upon vertical transfer of 222(31) nm particles onto a chip with Lumped Element Resonators at 55 mN/m.
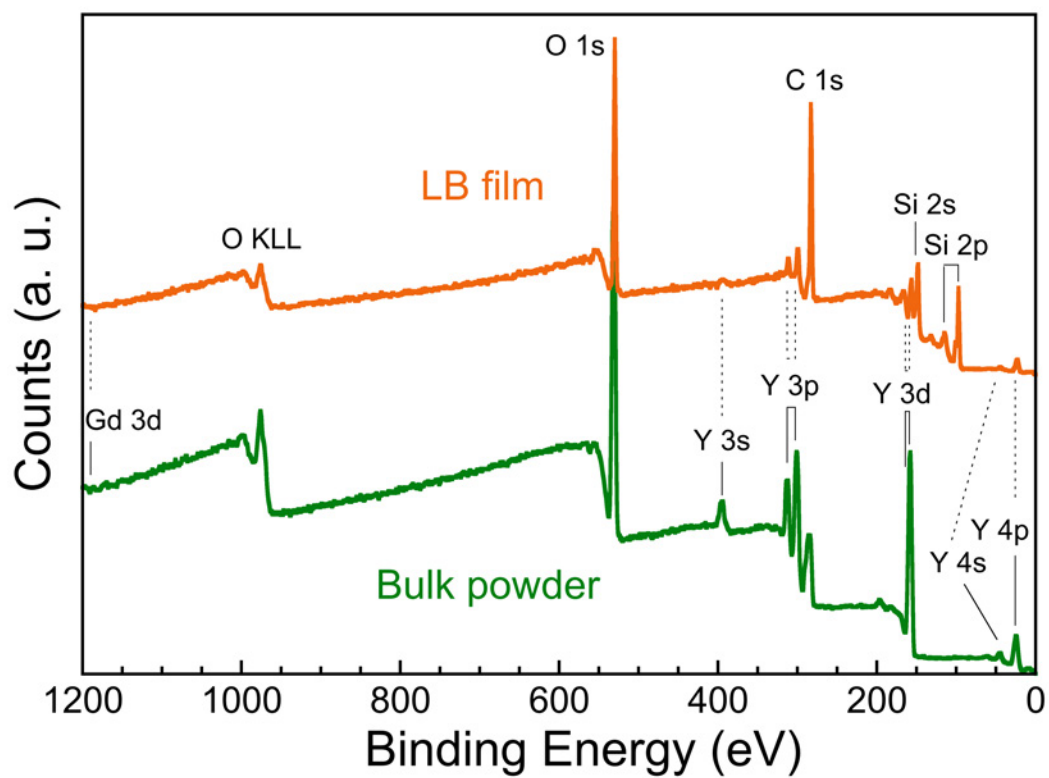
Figure S20. XPS survey spectra of a LB film of $Gd_{0.003}Y_{0.997}CO_3OH$ particles on Si (top) and of the same particles as bulk powder.
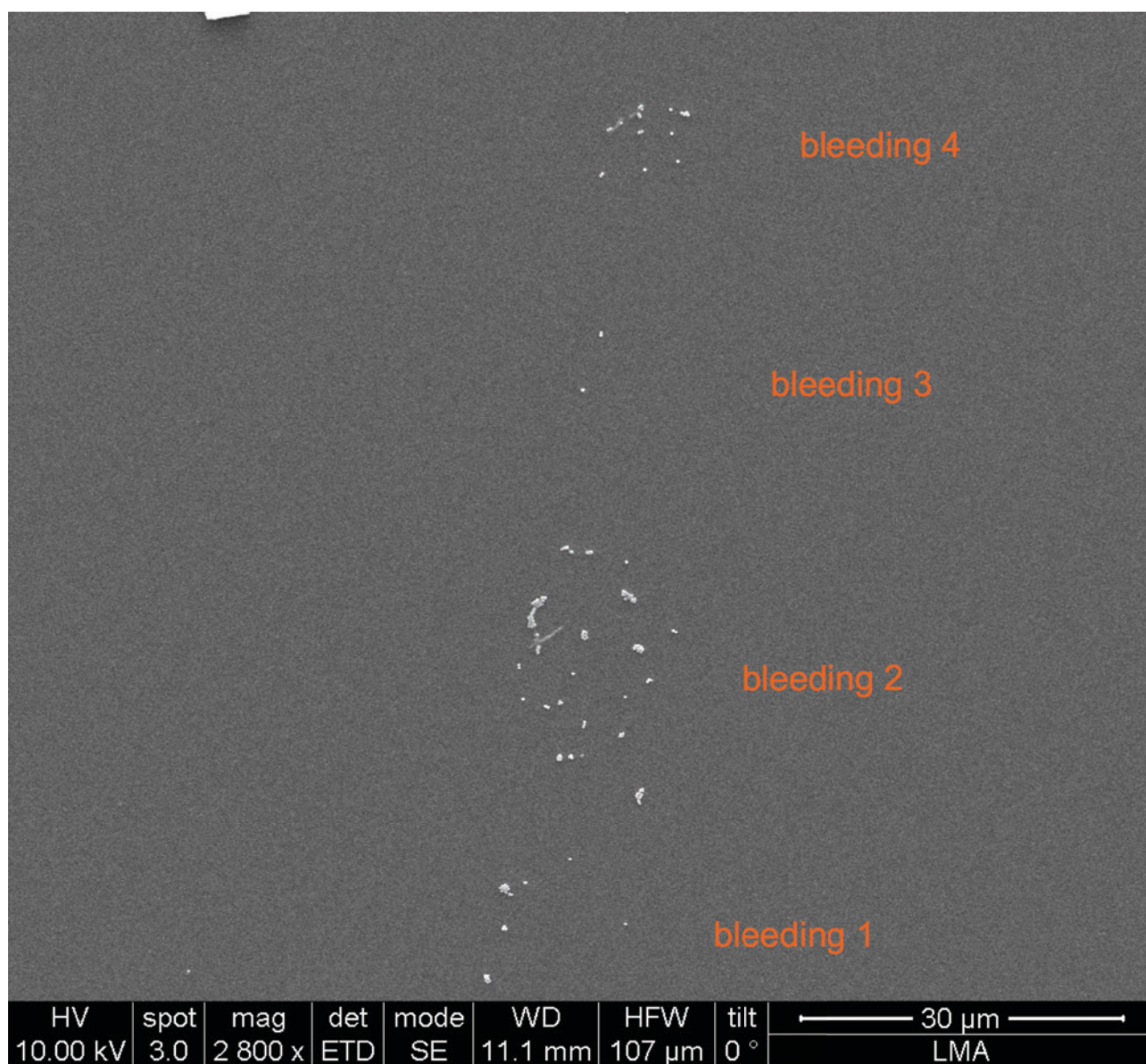
Figure S21. SEM image of four successive DPN cantilever bleeding steps after charging it with a 0.5 mg/mL DMF dispersion.
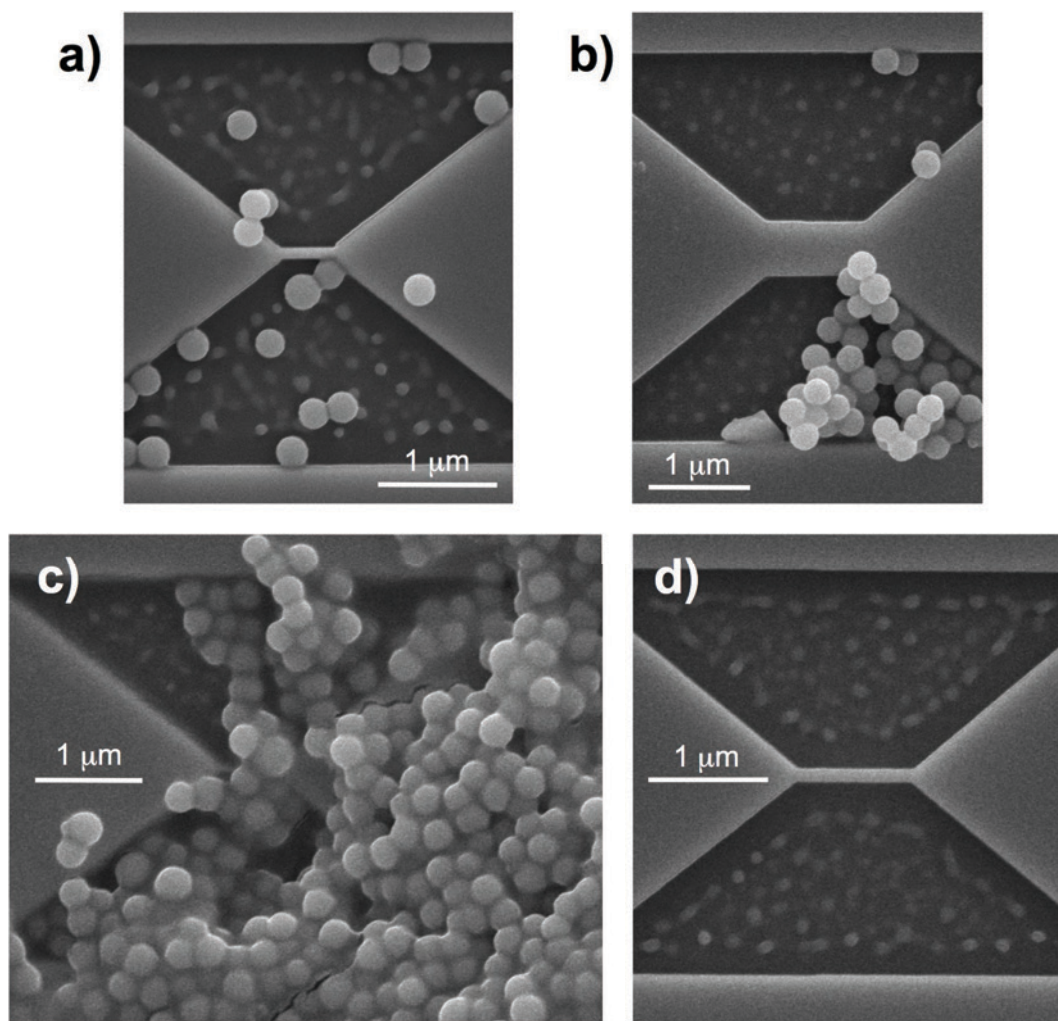
Figure S22. SEM images of various deposits made through AFM tip stamping in the vicinity of Nb nanoconstrictions in Nb, using a DMF dispersion of $Gd_{0.003}Y_{0.997}OHCO_3$ particles as ink: a) and b) are examples of deposits obtained using a strong tip-surface contact interaction after the excess ink carried by the cantilever has been reduced; c) corresponds to the case of a deposit obtained when the cantilever charge is excessive; d) represent the case of weak tip-surface interaction through the DMF, with no particles deposited.